On the Reynolds-number independence of mixed convection in a vertical channel subjected to asymmetric wall temperatures with and without flow reversal

Yih Nen Jeng and Jiann Lin Chen
Institute of Aeronautics and Astronautics, National Cheng Kung University, Tainan, Taiwan, Republic of China

Win Aung
Department of Mechanical Engineering and Mechanics, Drexel University, Philadelphia, PA, USA

The problem of mixed convection in a vertical channel with asymmetric wall temperatures including situations of flow reversal is studied numerically. The SIMPLER algorithm with a staggered grid system is employed to solve the corresponding numerical equations formulated by the finite-volume method. A second-order upwind scheme is used to model the convective term, and a suitable grid distribution is introduced. The ranges of the parameters studied are $0 \leqslant r_t \leqslant 1$, $1 \leqslant \mathrm{Re} \leqslant 1000$, and $0 \leqslant \mathrm{Gr/Re} \leqslant 500$.

The numerical results, with the streamwise coordinate scaled by the Reynolds number (Re), show that solutions for the velocity and temperature fields are independent of the Reynolds number when $\mathrm{Re} \geqslant 50$, even in the presence of flow reversal. These solutions, however, are dependent on r_t and Gr/Re. Subsequently, correlations are proposed for the bulk temperature distribution and the local Nusselt numbers along the hot wall and the cold wall.

Keywords: mixed convection; finite-volume method

Introduction

Mixed-convection heat transfer is important in many technical fields due to its frequent occurrence in industrial, technological, and natural surroundings. For example, heat transfer involving flow through a parallel-plate channel is found in conventional flat-plate-type solar collectors and equipment for electronic cooling. In the latter application, electronic components are normally mounted on parallel circuit boards, which are generally positioned vertically in a cabinet and form vertical parallel channels through which coolants are passed. The coolants may be propelled by free convection, forced convection, or mixed convection, depending on the power density of the circuit boards. The present investigation deals with a parallel-plate channel with asymmetric wall temperatures in which steady-state heat transfer characteristics are of interest.

Like the study of steady-state laminar free convection (Anand, Kim, and Aung 1990; Buck and Wood 1992; Sparrow, Chrysler, and Azevedo 1984; Nieckele and Azevedo 1987; Aung, Fletcher, and Sernas 1972; Yao 1983), steady laminar mixed convection in a vertical-plane channel has been extensively investigated by numerical methods (Aung and Worku 1986a, 1986b; Habchi and Acharya 1986; Ingham, Keen, and Heggs 1988; Mahmood and Merkin 1989; Cheng, Kou, and Huang 1990) and experimental methods (Wirtz and McKinley 1985). In these studies, the flow reversal was frequently considered. Sparrow and coworkers (1984) performed a combined numerical and experimental study on steady laminar free convection in a one-side heated vertical channel for a working fluid with $\mathrm{Pr} \sim 7.0$. Flow visualization conducted in their study reveals that, at a Rayleigh number that exceeds a threshold value, a pocket of recirculating flow exists adjacent to the unheated wall in the upper part of the channel. According to mass conservation, the recirculation is fed by fluid drawn from the top of the channel, adjacent to the unheated wall. They also showed that the Nusselt numbers at the heated wall are unaffected by the presence of the recirculation zone. Based on this condition, they employed the boundary-layer equation to predict the heat transfer properties. Nieckele and Azevedo (1987) used the elliptic-equation model rather than the boundary-layer model, so that the recirculating region was accurately simulated when compared with flow visualization. Though Sparrow and coworkers (1984) and Nieckele and Azevedo (1987) employed water as the working fluid ($\mathrm{Pr} = 5 \sim 7$), it is believed that their results are qualitatively valid for air ($\mathrm{Pr} = 0.7$).

Wirtz and McKinley (1985) performed the mixed-convection experiment and discussed the buoyancy effect in a laminar downflow of air between two vertical parallel plates. One plate had a uniform wall heat flux while the other was unheated. The wall heat flux was increased until the flow between the plates

Address reprint requests to Professor Jeng at the Institute of Aeronautics and Astronautics, National Cheng Kung University, Tainan, Taiwan, Republic of China.

Received 4 October 1991; accepted 19 April 1992

became three-dimensional (3-D), indicating the onset of flow reversal. Local heat transfer measurements showed that the overall heat transfer coefficient first decreased with increasing Grashof number, then increased at higher heat fluxes.

In principle, the governing momentum and energy equations are elliptic in nature; hence, the resulting numerical equations should be solved by iterative techniques. If the Reynolds and Peclet numbers are relatively large, after a suitable non-dimensionalization process, the spanwise diffusion terms in the momentum and energy equations can be much more important than the axial diffusion terms. Neglecting the axial diffusion terms makes the Navier–Stokes and energy equations parabolic in nature. The resulting equations may then be solved by a much simpler marching procedure. For parabolic equations, the marching techniques were successively employed in the models of Aung, Fletcher, and Sernas (1972), Aung and Worku (1986a, 1986b), Buck and Wood (1992), Habchi and Acharya (1986), and Ingham, Keen, and Heggs (1988), among others.

By employing the FLARE approximation (Bradshaw, Cebeci, and Whitelaw 1981; Williams 1975), most of the above solutions can be further extended to include the region of flow reversal. The present authors have performed a test run by repeating the work of Aung and Worku (1986a) by the FLARE approximation, and the results have been compared with those of the present elliptic model. Although the resulting velocity and temperature fields are not correctly predicted, it is found that the Nusselt numbers are adequately predicted even in the presence of flow reversal. Consequently, it seems that these marching techniques can handle the mixed-convection problem, at least for engineering applications. The remaining issue is the limitation of these marching techniques.

So far, no study has been carried out on the limiting Reynolds number below which a marching technique will lead to significant error. In this article, the full Navier–Stokes equations along with the energy equation will be employed to address this issue. The capability of predicting the local Nusselt numbers by the marching technique of Aung and Worku (1986a) will also be demonstrated.

The physical model considered here is shown in Figure 1, where uniform entrance conditions are assumed. Note that the magnitude of the inlet velocity is a given quantity. It is assumed that in the physical situation, the fan or blower is adjusted to maintain the given velocity when flow rate is modulated by mixed convection. The governing equations based on the finite-volume method (see Morton and Paisley 1989; Vinokur 1989) are solved using the SIMPLER algorithm and a staggered grid system (Patankar 1980; Harlow and Welch 1965), along with a more suitable grid distribution that is in accordance with error analysis (Jeng and Chen 1992; Turkel 1986). Note that, for a Cartesian grid system, the finite-volume method is

Notation

A Coefficient in Equation A7
b Channel width
Gr Grashof number
g Magnitude of the gravitational acceleration
$\vec{h}$ Convective heat transfer coefficient
i, j Unit vector for x, y coordinates, respectively
IAE $=[\int_0^{L_X} |\tilde{\theta}_b(x) - \theta_b(x)|\,dx]/L_X$
k Thermal conductivity
l Local mesh spacing
L_s $=\dfrac{x_s}{\mathrm{Re}}$
L_x $=\min\left[\dfrac{x_{max}}{\mathrm{Re}}, \dfrac{\tilde{x}_{max}}{\tilde{\mathrm{Re}}}\right]$
MAE $=\max|\tilde{\theta}_b(x) - \theta_b(x)|$
MSE $=[\sum_i(\tilde{\theta}_b(x) - \theta_b(x))^2]^{1/2}/i_{max}$, summation over all the x-grid points
Nu Local Nusselt number, Equation 10b
p Dimensionless local pressure
p' Pressure correction in SIMPLER algorithm
$\bar{p}$ Local pressure
Pr Prandtl number of air (=0.72)
R Grid stretching ratio
Re Reynolds number
r_t Dimensionless temperature at cold wall
$\vec{T}$ Temperature
S Cell surface vector
S Source term
u, v Dimensionless velocities
$\bar{u}, \bar{v}$ Velocities
$\vec{V}$ $V = ui + vj$ in Equation A1
v Control volume
x, y Dimensionless coordinates
$\bar{x}, \bar{y}$ Coordinates on physical domain
x_{max} The computed domain
$\tilde{x}_{max}$ The computed domain for reference $\tilde{\mathrm{Re}}$
x_s The separation distance from the channel entrance

Greek symbols
α Thermal diffusivity of air
β Coefficient of thermal expansion of air
Γ Diffusion coefficient in Equation A1
Δ Grid spacing, e.g., $\Delta x_{12} = x_2 - x_1$
ξ, η Coordinates on transformed domain
ρ Density of air
ε Constant in Equation A9
θ Dimensionless temperature
$\tilde{\theta}_b(x)$ The local bulk temperature for reference $\tilde{\mathrm{Re}}$
ν Kinematic viscosity of air
ϕ Dependent variable
∇ $\dfrac{\partial}{\partial x}\vec{i} + \dfrac{\partial}{\partial y}\vec{j}$

Subscripts
0 Entrance
1, 2, 3, 4 Vertices of main control volume
b Bulk
c Cold wall ($y = 1$)
f Exact solution at fully developed region
h Hot wall ($y = 0$)
i, j Grid node indices
P Node of main control volume
e Right vertical control-volume surface center
E Node to the right of main control volume
max x_{max} is location of the downstream boundary
n Top horizontal control-volume surface center
N Node to the top of main control volume
s Bottom horizontal control-volume surface center
S Node to the bottom of main control volume
w Left vertical control-volume surface center
wq Wall with uniform heat flux
W Node to the left of main control volume

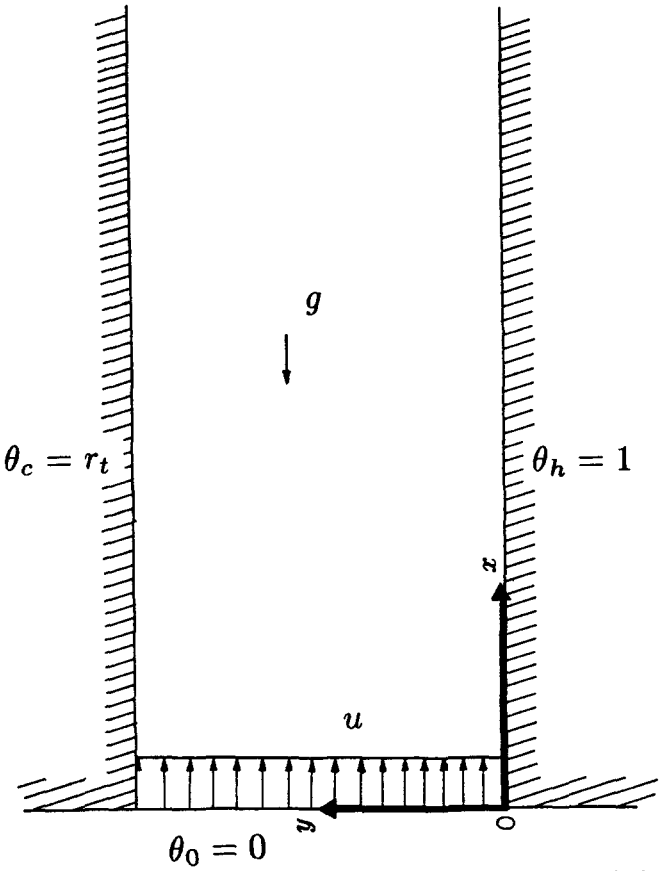

Figure 1 The physical model of mixed convection in a vertical channel

the same as the control-volume-based finite-difference method. For a generalized grid system, the analogy between these two methods still exists, except that there are some departures in evaluating metric coefficients (Jeng and Chen 1992). The classical second-order upwind scheme (Shyy 1985a; Vanka 1987), which introduces less false diffusion, is adopted to model the convective terms in the present calculation.

Numerical methodology

The governing equations

The nondimensional Navier–Stokes equations and the boundary conditions that describe the physical situation as shown in Figure 1 are written in the Cartesian coordinate system as follows:

$$\frac{\partial u}{\partial x} + \frac{\partial v}{\partial y} = 0 \tag{1}$$

$$u\frac{\partial u}{\partial x} + v\frac{\partial u}{\partial y} = -\frac{\partial p}{\partial x} + \frac{\mathrm{Gr}}{\mathrm{Re}^2}\theta + \frac{1}{\mathrm{Re}}\left(\frac{\partial^2 u}{\partial x^2} + \frac{\partial^2 u}{\partial y^2}\right) \tag{2}$$

$$u\frac{\partial v}{\partial x} + v\frac{\partial v}{\partial y} = -\frac{\partial p}{\partial y} + \frac{1}{\mathrm{Re}}\left(\frac{\partial^2 v}{\partial x^2} + \frac{\partial^2 v}{\partial y^2}\right) \tag{3}$$

$$u\frac{\partial \theta}{\partial x} + v\frac{\partial \theta}{\partial y} = \frac{1}{\mathrm{Re}\cdot\mathrm{Pr}}\left(\frac{\partial^2 \theta}{\partial x^2} + \frac{\partial^2 \theta}{\partial y^2}\right) \tag{4}$$

$x = 0,\ 0 \leqslant y \leqslant 1$: $u = 1,\ v = 0,\ \theta_0 = 0,\ p = 0$

$0 < x < x_{\max},\ y = 0$: $u = 0,\ v = 0,\ \theta_h = 1$

$0 < x < x_{\max},\ y = 1$: $u = 0,\ v = 0,\ \theta_c = r_t$

where

$$u = \frac{\bar{u}}{\bar{u}_0},\ v = \frac{\bar{v}}{\bar{u}_0},\ p = \frac{\bar{p}}{\rho\bar{u}_0^2},\ \theta = \frac{T - T_0}{T_h - T_0},\ x = \frac{\bar{x}}{b},\ y = \frac{\bar{y}}{b}$$

The Boussinesq approximation for the buoyancy force term has been employed (Aung and Worku 1986a) and the Reynolds number, Grashof number, and Prandtl number are defined as $\mathrm{Re} = \bar{u}_0 b/\nu$, $\mathrm{Gr} = g\beta(T_h - T_0)b^3/\nu^2$, and $\mathrm{Pr} = \nu/\alpha$, respectively. When Gr is positive, it is a buoyancy aiding flow; otherwise, it is an opposing flow.

Recall that the exact solution of the fully developed flow of Aung and Worku (1986b) used Gr/Re and $\mathrm{Re}(\partial p/\partial x)$ as parameters. The boundary-layer approximation of Aung and Worku (1986a) also used the dimensionless parameter Gr/Re rather than the parameter $\mathrm{Gr}/\mathrm{Re}^2$ in the governing Navier–Stokes equations (Equations 1 to 4). Moreover, in the situation without flow reversal, the numerical solution found by the boundary-layer approximation agrees with the experimental data and is independent of the Reynolds number (Aung and Worku 1986a). These experiences indicate that the Reynolds number is not an explicit parameter whenever the number is large enough. To look into this problem, we use the following nondimensionalized variables (Aung and Worku 1986a):

$$u = \frac{\bar{u}}{\bar{u}_0},\ v = \frac{\bar{v}b}{\nu},\ p = \frac{\bar{p}}{\rho\bar{u}_0^2},\ \theta = \frac{T - T_0}{T_h - T_0},\ x = \frac{\bar{x}}{b\cdot\mathrm{Re}},\ y = \frac{\bar{y}}{b}$$

to transform the governing equations (Equations 1 to 4) to

$$\frac{\partial u}{\partial x} + \frac{\partial v}{\partial y} = 0 \tag{5}$$

$$u\frac{\partial u}{\partial x} + v\frac{\partial u}{\partial y} = -\frac{\partial p}{\partial x} + \frac{\mathrm{Gr}}{\mathrm{Re}}\theta + \frac{1}{\mathrm{Re}^2}\frac{\partial^2 u}{\partial x^2} + \frac{\partial^2 u}{\partial y^2} \tag{6}$$

$$u\frac{\partial v}{\partial x} + v\frac{\partial v}{\partial y} = -\mathrm{Re}^2\frac{\partial p}{\partial y} + \frac{1}{\mathrm{Re}^2}\frac{\partial^2 v}{\partial x^2} + \frac{\partial^2 v}{\partial y^2} \tag{7}$$

$$u\frac{\partial \theta}{\partial x} + v\frac{\partial \theta}{\partial y} = \frac{1}{\mathrm{Pr}}\left(\frac{1}{\mathrm{Re}^2}\frac{\partial^2 \theta}{\partial x^2} + \frac{\partial^2 \theta}{\partial y^2}\right) \tag{8}$$

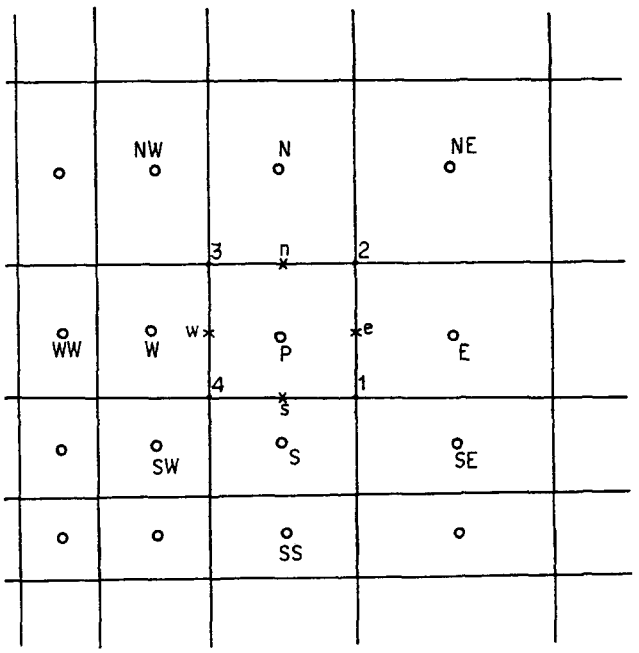

Figure 2 The node arrangement on rectangular cells

Obviously, as $\mathrm{Re} \to \infty$, the terms multiplied by $1/\mathrm{Re}^2$ are negligible, so that these equations become a set of parabolized Navier–Stokes equations. Further, except for the inlet region, terms other than $\partial p/\partial y$ are moderate in magnitude, so that Equation 7 becomes

$$\frac{\partial p}{\partial y} \sim \mathrm{O}\left(\frac{1}{\mathrm{Re}^2}\right) \tag{9}$$

Consequently, the boundary-layer approximation is valid at regions other than the inlet region. Note that the boundary-layer equation will induce another error near the point of separation for the case with flow reversal.

The above discussion shows that, when Re is large enough, the velocity and temperature fields are governed by the two parameters Gr/Re and Pr, and are nearly independent of Re. In this study, we will focus on the independence of the solutions on Re.

Definitions of the Nusselt number

Basically, the local Nusselt number at a location $\bar{x}$, which is defined based on the energy balance by Özisik (1985), can be derived as follows:

$$h(T_b - T_0) = -k \left.\frac{\partial T}{\partial \bar{y}}\right|_{\text{wall}} \tag{10a}$$

$$\mathrm{Nu}\Big|_{\text{wall}} = \frac{hb}{k} \tag{10b}$$

For a channel flow with asymmetric uniform wall temperatures, Nu for the hot wall ($y = 0$) and cold wall ($y = 1$) can be defined, respectively, by

$$\mathrm{Nu}\Big|_{y=0} = -\frac{1}{\theta_b}\left.\frac{\partial \theta}{\partial y}\right|_{y=0} \tag{11a}$$

$$\mathrm{Nu}\Big|_{y=1} = \frac{1}{\theta_b}\left.\frac{\partial \theta}{\partial y}\right|_{y=1} \tag{11b}$$

The SIMPLER algorithm with a staggered grid system, as shown in Figure 2, is employed to solve the corresponding numerical equations (Equations 1 to 4) formulated by the finite-volume method (Jeng and Chen 1992). The second-order upwind scheme is used to model the convective term. For the sake of clarity, the finite-volume formulation for a model equation is derived in Cartesian coordinates and given in Appendix 1.

For the numerical solutions, the inflow boundary conditions are specified. In order to investigate the effect of open-boundary conditions on the problem of well-posedness for steady incompressible Navier–Stokes equations, Shyy (1985b, 1987) performed a series of numerical experiments. He found that the first-order extrapolation approximation, say $\phi_\xi = 0$, on an open boundary was sufficient to provide the well-posedness even if the open boundary has flow reversal. Therefore, for boundary conditions at $x = L/b = x_{\max}$, the following first-order extrapolation recommended by Shyy (1985b, 1987) has been invoked:

$$\phi^{n+1}_{i_{\max}} = \phi^{n}_{i_{\max}-1}, \quad \phi = u, v, \quad \text{or} \quad \theta \tag{12}$$

where the superscript n is the number of iteration steps. Moreover, it is noted that a staggered grid arrangement is suitable for the present treatment of boundary conditions, especially for the pressure and pressure-correction equations (Patankar 1980).

The present physical problem requires that the grid be refined in the entrance region as well as the wall regions to handle the large gradients expected there. This requirement can be easily satisfied by a rectangular grid system with proper stretching along grid lines. Here, the one-dimensional (1-D) grid-stretching method of Sorenson and Steger (1977) is used. For the sake of completeness, their method is briefly described in Appendix 2.

Results and discussion

The validation of numerical simulation

To check the validity of the program, a high-Reynolds-number forced-convection flow between parallel flat plates, which was analytically solved by Heaton, Reynolds, and Kays (1964), is first considered. One wall is heated at uniform heat flux and the other is adiabatic. The analytic solution is independent of the Reynolds number.

In the present study, numerical solutions are obtained for Reynolds numbers of 1,000 (with 151 × 41 algebraic stretched grids) and 660 (with 121 × 41 algebraic stretched grids). The results are shown in Figure 3. The agreement between the exact solution and the two numerical solutions (with streamwise coordinate being properly scaled) is obvious.

The second test problem uses the experimental data of Aung et al. (1986a), where $\mathrm{Gr/Re} = 23.44$ and $r_t = 0.33$. Figure 4 displays the local Nusselt numbers along the hot and cold walls. The quantity 2.2 in the streamwise coordinate in Figure 4 results from using different dimensionless groups in this study from those used by Aung and Worku (1986a) in which a characteristic channel length was employed. Numerical calculations are obtained for two different Reynolds numbers, and the two sets of results nearly coincide with each other. As may be seen, both sets of numerical results are close to the experimental data.

The third test case is the experimental study of mixed convection by Wirtz and McKinley (1985) for $\mathrm{Gr} = -8.1 \times 10^5$, $\mathrm{Pr} = 0.72$, and $\mathrm{Re} = 660$. Since the Grashof number is negative, the experiments deal with a buoyancy opposing flow with reversed flow at the exit, which is located at an axial distance that is about 10 times the channel width b. The numerical solution uses a 121 × 41 algebraically stretched grid. Two different locations of the outflow boundary (say, $x_{\max} = 10b$ and $15b$), which are at or beyond the point of separation, are computed. The results are plotted in Figure 5. The agreement

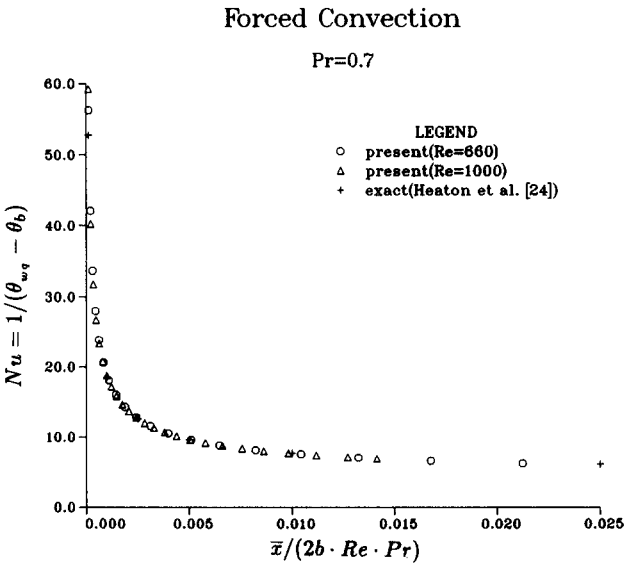

Figure 3 The comparisons of Nu with an exact solution and present results from two Reynolds numbers for forced convection

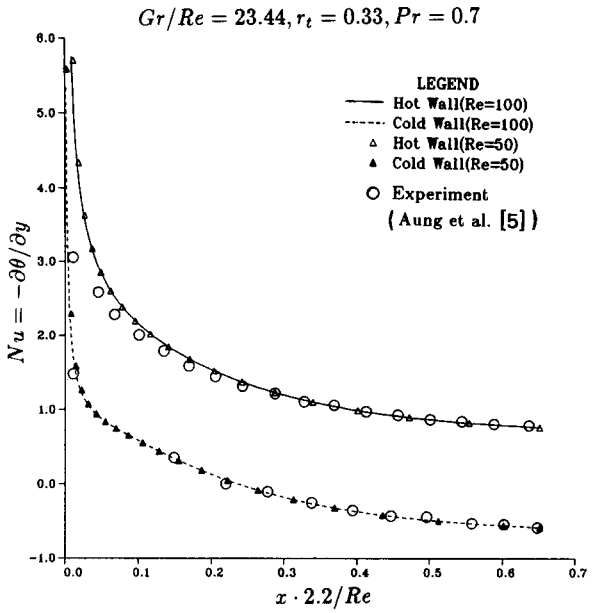

Figure 4 The comparisons of Nu from two Reynolds numbers with an experiment for mixed convection

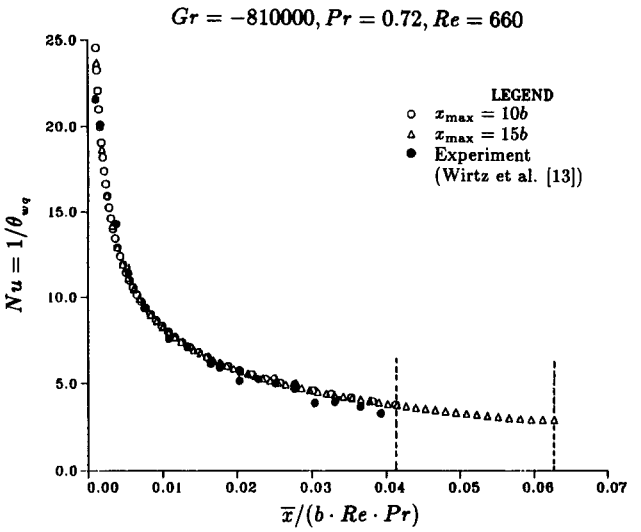

Figure 5 The comparisons of Nu from two computed domains with an experiment for mixed convection

between the experimental data and the two numerical solutions not only verifies the validity of the program but also shows that the outflow boundary conditions are reliable.

To demonstrate the merit of grid stretching, the mixed-convection problem between vertical parallel plates with Re = 1, Pr = 0.72, r_t = 0.5, and Gr/Re = −140 is considered. At these flow conditions, the numerical solution of the perturbed Navier–Stokes equations (Ingham, Keen, and Heggs 1988) shows that there is a separation bubble at the hot wall. Figure 6a shows the numerical solution using a 121 × 41 uniform grid system, where a separation bubble is found near the right boundary (hot wall). The solution using 61 × 21 uniform grid as shown in Figure 6b, however, cannot capture the recirculation zone. The reason is that the thickness of the separation bubble is slightly smaller than the grid spacing next to the wall boundary. When the grid lines are algebraically stretched and the grid spacing next to the wall boundary is small enough, the recirculation

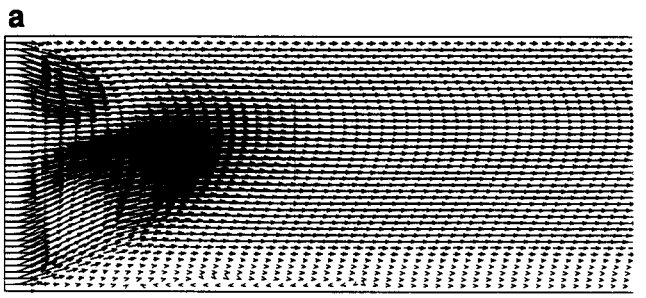

Figure 6(a) The results from uniform grids 121 × 41 (flow reversal occurs at the hot wall)

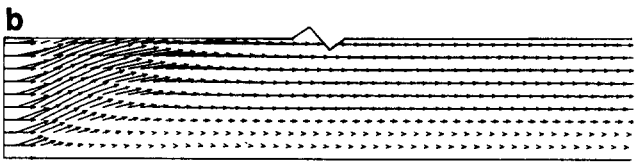

Figure 6(b) The results from uniform grids 61 × 21 (no flow reversal occurs at the hot wall)

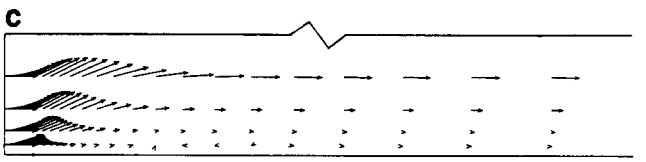

Figure 6(c) The results from stretched grids 31 × 11 (flow reversal occurs at the hot wall)

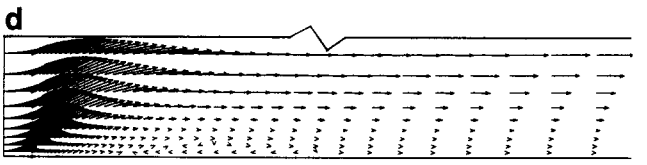

Figure 6(d) The results from stretched grids 61 × 21 (flow reversal occurs at the hot wall)

zone can be properly captured. This point is further illustrated in Figures 6c and 6d, which display the results using 31 × 11 and 61 × 21 stretched grid systems, respectively. In each case, the separation zone is captured at the hot wall. The case involving the coarser grids, however, is not one of algebraic stretched grids, since ε of Equation A12 (that is, ε = 0.2) is not small enough, so that both the location and the size of the recirculation zone are not properly resolved. This test case shows that a grid system with suitable grid stretching can give better resolution.

In the remainder of this article, results obtained with the 121 × 41 grid system using algebraic stretching will be described. All the solutions shown meet the requirement of grid independence. The convergence criterion, based on the residues of the numerical equations (Equation A7) as well as variations of pressure and temperature between two successive iterations, are set at less than 5×10^{-7}. The ranges of the relevant parameters investigated are $0 \leqslant r_t \leqslant 1$; $1 \leqslant Re \leqslant 1000$; $0 \leqslant Gr/Re \leqslant 500$.

Comparison with solutions of boundary-layer approximation

The discussion following Equation 9 indicates that a solution using the boundary-layer approximation will induce error at

the inlet region. As an illustration, consider a typical example at Re = 10, Gr/Re = 300, and $r_t = 0.3$, as shown in Figure 7, where flow reversal is found. The computation length is up to 10 times the channel width b. The velocity distribution at various locations are shown in Figure 8. At the inlet region and the region around the separation point, the assumptions of the boundary-layer approximation (Aung, Fletcher, and Sernas 1992; Aung and Worku 1986a) of $u \gg v$ and $(\partial u/\partial y) \gg (\partial u/\partial x)$ are no longer valid. However, at a downstream distance about $3b$ or $4b$ from the separation point, the boundary-layer approximation seems to become valid again. It should be pointed out that these errors become smaller as the Reynolds number increases.

To estimate this error at higher Reynolds numbers, some of the cases investigated in Aung and Worku (1986a) are recalculated. Owing to stability problems in their study, Aung and Worku (1986a) do not give the results downstream of the separation points. Figure 9 compares the boundary-layer approximations in Aung and Worku (1986a) with the present solutions (Re = 100) at Gr/Re = 250. It is clear that the boundary-layer approximation cannot accurately simulate the entrance and separation regions. For the situation in which the separation point is remote from the entrance, the accumulated error of the boundary-layer approximation can negatively influence the accuracy of the prediction near the separation point. Therefore, as shown in Figure 9, the predicted locations of the separation point for the two solutions are in agreement for $r_t = 0.3$, but deviate from each other for $r_t = 0.5$. However, the boundary-layer solutions for the bulk temperature deviate only slightly from the present solutions. It seems that the marching technique is a good approach for estimating the heat transfer for engineering applications.

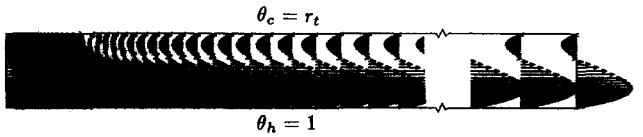

Figure 7 The flow field of Re = 10, Gr/Re = 300, and $r_t = 0.3$

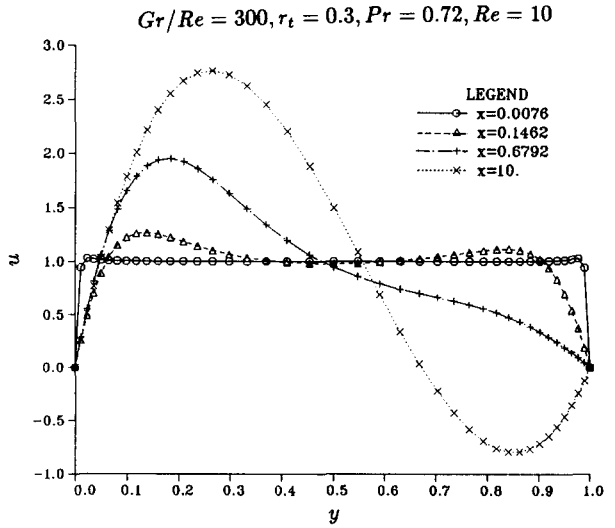

Figure 8 The velocity profiles at various locations for Re = 10, Gr/Re = 300, and $r_t = 0.3$

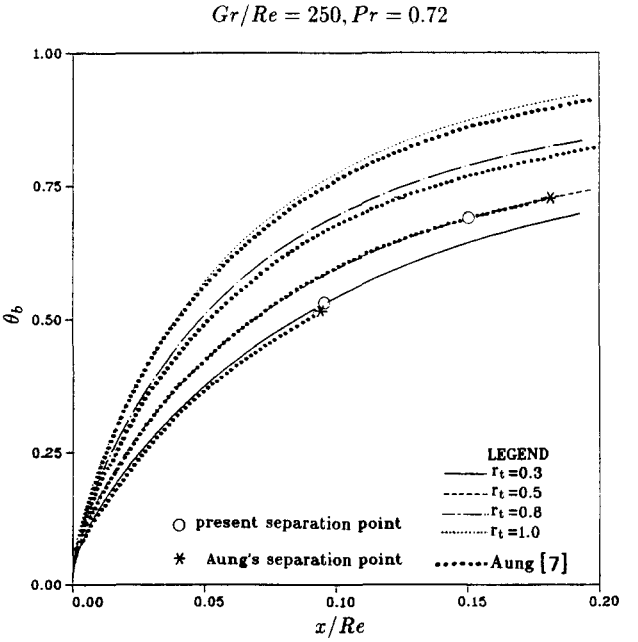

Figure 9 The comparisons of present θ distributions from various values of r_t with Aung's boundary-layer solutions

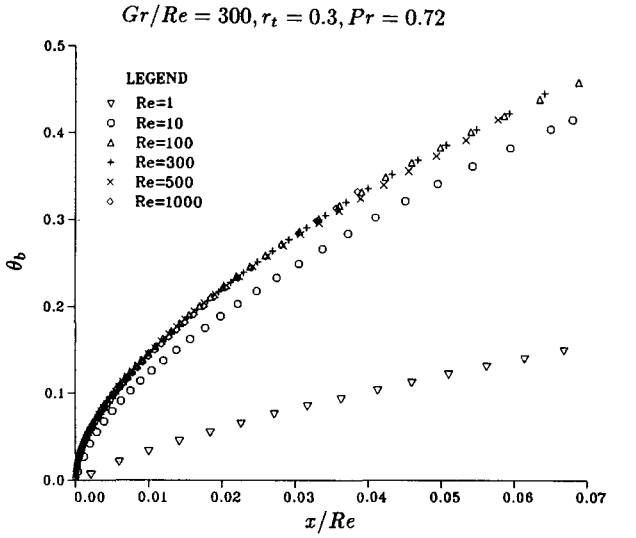

Figure 10 The θ_b distributions against x/Re for various values of Re

The Reynolds-number independence

The numerical test cases and the corresponding experimental data show that the results of these problems do not explicitly depend on the Reynolds number. Using Equations 5 to 8, it is possible to seek the lower limit of the Reynolds number above which the results are independent of Re. In this section, numerical experiments have been used to approach this problem. Without loss of generality, a specific case involving flow reversal has been chosen to demonstrate the independence of the solutions to the Reynolds number. Once this is demonstrated, it is then possible to extend the results to cases without flow reversal.

Figure 10 shows the bulk temperature distributions for different values of Re at Gr/Re = 300, $r_t = 0.3$. The streamwise

Table 1 Comparison of discrepancy for various Re numbers based on reference $\widetilde{Re}$ = 1,000 for Gr/Re = 300 and $r_t = 0.3$

Re	L_X	MAE	MSE	IAE	L_s
1	0.04	0.14509	0.08293	0.08215	0.43233
10	0.04	0.03792	0.00383	0.02565	0.10658
25	0.04	0.00686	0.00056	0.00338	0.09474
50	0.04	0.00571	0.00057	0.00252	0.09244
75	0.04	0.00596	0.00058	0.00317	0.09221
100	0.04	0.00560	0.00050	0.00318	0.09211
150	0.04	0.00475	0.00042	0.00269	0.09200
200	0.04	0.00401	0.00034	0.00221	0.09213
300	0.04	0.00282	0.00023	0.00159	*
500	0.04	0.00174	0.00012	0.00106	*
1000	0.04				*

* No separation is found within the computed domain x_{max}.

coordinate x in Equations 1 to 4 is scaled to be x/Re, which is then the same as the streamwise coordinate of Equations 5 to 8. Clearly, for Re $\geqslant$ 100, the bulk temperature distributions collapse to a single line.

Using the solution for Re = 1000 as a standard, solutions for all the Re's at Gr/Re = 300 and $r_t = 0.3$ are compared from x/Re = 0 to 0.04, as shown in Table 1. The table shows their departures based on the l_∞-norm of the difference (MAE), the l_2-norm of the difference (MSE), and the approximate L_1-norm of the difference (IAE). The last norm of the difference is employed because it reflects the factor of x/Re. Also shown is the distance from the channel entrance to the separation point. As Re increases, the location of the separation point appears to converge to a single value. The slight increase at Re = 200 is probably due to the effect of the exit boundary condition, since the exit plane (x_{max}/Re = 0.1) is close to the separation point. For Re $\geqslant$ 300, the computed domains do not cover the separation point.

Table 1 shows that, for Re $\geqslant$ 50, the resulting bulk temperature distributions are close to that for Re = 1,000. Moreover, the locations of the separation points agree to within two digits.

The streamline contours for different values of Re at Gr/Re = 300 and $r_t = 0.3$ show that the flow pattern at low Re is quite different from that for Re $\geqslant$ 50. Despite differences in the computational domain, for Re $\geqslant$ 50, all streamline contours coincide with each other within the graphical drawing error. Similar conclusions may be drawn for the isotherms. That is, for Re $\geqslant$ 50, all isothermal contours coincide with one another.

By inspecting Figure 10 and Table 1, it may be concluded that with Gr/Re = 300 and $r_t = 0.3$, the limiting Reynolds number above which the velocity and temperature fields are independent of the Reynolds number is about Re $\sim$ 50. For other parameters, as shown in Appendix 3, the results also support the same conclusion. By virtue of the comparison in Figure 9, it seems that the marching techniques of Aung and Worku (1986a) is acceptable in predicting the heat transfer for laminar flow with Re > 50.

The location of the separation point measured from entrance versus Gr/Re for various values of r_t at Re = 100 is shown in Figure 11. It is obvious that the higher the Gr/Re and/or r_t, the smaller the value of L_s.

The correlations for θ_b and Nu

Examination of Figure 10 reveals that the bulk temperature increases rapidly immediately downstream of the channel entrance. Further downstream, the increase with distance is more gradual. The relationship between the bulk temperature and Gr/Re, r_t at distances far downstream of the channel entrance has been derived by Aung and Worku (1986b). This is the so-called fully developed flow solution. Moreover, from the bulk temperature distribution of Figure 9, the results indicated in Aung and Worku (1986a), and the numerical results not shown here, it is found that the bulk temperature and the local Nusselt number distributions are similar to each other. It is possible to collapse each set of results if x is properly scaled. Consequently, it is possible to derive correlations for θ_b and Nu.

In the present study, correlations for θ_b and Nu have been derived by using the results for θ_b indicated in Aung and Worku (1986b). The corresponding expression for Nu_f can be easily derived and is shown below.

For the bulk temperature distribution, the vertical axis uses the normalized variable θ_b/θ_{bf}, and the horizontal axis employs the variable $x/\mathrm{Re}\cdot Sc$). The relevant parameters are

$$Sc = \left(1 - 0.5\left(\frac{\mathrm{Gr/Re}}{1000}\right)^{0.7}\right)(1 + c_1(1 - r_t)^{c_2}) \tag{13a}$$

$$c_1 = 0.0316(\mathrm{Gr/Re})^2 + 0.222(\mathrm{Ge/Re}) \tag{13b}$$

$$c_2 = 0.1125(\mathrm{Gr/Re})^2 - 1.2(\mathrm{Gr/Re}) + 4.5875 \tag{13c}$$

$$\theta_{bf} = \frac{1}{720}(\mathrm{Gr/Re})(1 - r_t)^2 + \tfrac{1}{2}(1 + r_t) \tag{13d}$$

where θ_{bf} is obtained from Aung and Worku (1986a).

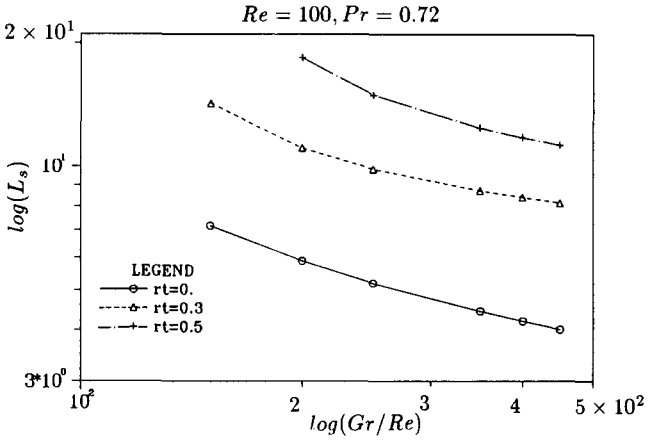

Figure 11 Predicted separation-point location versus various Gr/Re for different r_t

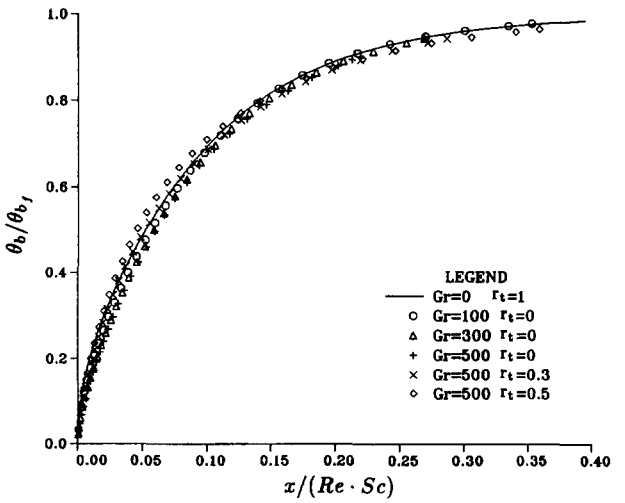

Figure 12 The correlation for bulk temperature

For the Nusselt number along the hot wall, the vertical axis is $Nu-Nu_f$ and the horizontal axis is $x/(Re\cdot Sc1)$, where

$$Sc1 = \left(1 - 0.5\left(\frac{Gr/Re}{1000}\right)^{1.2}\right)(1 + c_1(1 - r_t)^2) \quad (14a)$$

$$c_1 = -0.08(Gr/Re)^2 + 0.68(Gr/Re) \quad (14b)$$

$$Nu_f = \frac{1 - r_t}{\theta_{bf}} \quad (14c)$$

For the Nusselt-number distribution at the cold wall, the vertical axis is $Nu + Nu_f$, and the horizontal axis is $x/(Re\cdot Sc2)$, where

$$Sc2 = \left(1 - 0.3\left(\frac{Gr/Re}{1000}\right)^{1.2}\right)(1 + c_1) \quad (15a)$$

$$c_1 = 0.017(Gr/Re)^2 - 0.151(Gr/Re) \quad (15b)$$

$$Nu_f = \frac{1 - r_t}{\theta_{bf}} \quad (15c)$$

Figures 12, 13a, and 13b show the graphical representation of the correlations for normalized bulk temperature and Nusselt numbers at the hot and cold wall, respectively. The solid curves in these figures are the solutions for forced convection ($Gr/Re = 0$) and $r_t = 1$. In each case, the parameters of Equations 13 to 15 make it possible for all data in the present study to collapse approximately into a single curve given by the solution for forced convection. It is noted that the case of $r_t = 0$ is not involved in the correlation of Figure 13b owing to the present definition of Nu. Consequently, these three correlations cover the ranges of $0 \leqslant r_t \leqslant 1$, $0 \leqslant Gr/Re \leqslant 500$ for laminar flows with $Re \geqslant 50$, except the case of $r_t = 0$ for Nu on the cold wall.

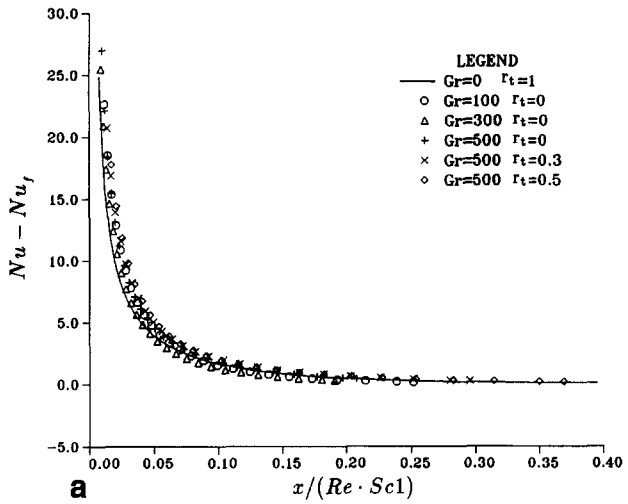

Figure 13(a) The correlation for Nu at the hot wall

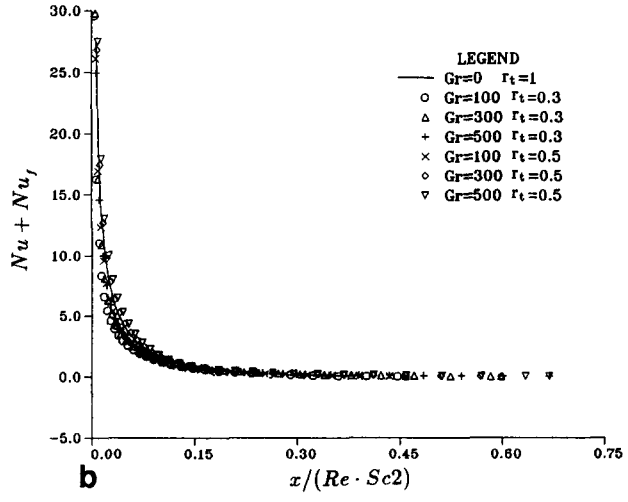

Figure 13(b) The correlation for Nu at the cold wall

Conclusions

Mixed convection between vertical parallel flat plates with and without flow reversal has been examined over the range of $Re = 1 \sim 1000$. A comparison between the present numerical solutions and those in Aung and Worku (1986a) indicates that the marching technique using the boundary-layer equations can accurately calculate the heat transfer on the heated wall. It is found that both the momentum and thermal characteristics are independent of Re for $Re \geqslant 50$ at fixed Gr/Re and r_t, if the streamwise coordinate x is scaled by Re. In other words, if $Re > 50$, the marching technique is a good approach for estimating the heat transfer for engineering applications. Based on the numerical solutions and the parameters of Gr/Re and r_t, correlations for the bulk temperature, the Nusselt number at the hot wall, and the Nusselt number on the cold wall versus x/Re have been proposed. The present results are valid in the ranges $0 \leqslant r_t \leqslant 1$, $1 \leqslant Re \leqslant 1{,}000$, and $0 \leqslant Gr/Re \leqslant 500$.

References

Anand, N. K., Kim, S. H., and Aung, W. 1990. Effect of wall conduction on free convection between asymmetrically heated vertical plates: uniform wall temperature. *Int. J. Heat Mass Transfer*, **33**, 1025–1028

Aung, W., Fletcher, L. S., and Sernas, V. 1972. Developing laminar free convection between vertical flat plates with asymmetric heating. *Int. J. Heat Mass Transfer*, **15**, 2293–2308

Aung, W. and Worku, G. 1986a. Developing flow and flow reversal in a vertical channel with asymmetric wall temperature. *ASME J. Heat Transfer*, **108**, 299–304

Aung, W. and Worku, G. 1986b. Theory of fully developed combined convection including flow reversal. *ASME J. Heat Transfer*, **108**, 485–488

Bradshaw, P., Cebeci, T., and Whitelaw, J. H. 1981. *Engineering Calculation Methods for Turbulent Flow*. Hemisphere, Washington, DC, 134

Buck, G. A. and Wood, B. D. 1992. A numerical investigation of natural convection heat and mass transfer from uniformly heated falling films in vertical channels. Presented at ASME Solar Energy Conference, Honolulu, Hawaii, April 4–8

Cheng, C. H., Kou, H. S., and Huang, W. H. 1990. Flow reversal and heat transfer of fully developed mixed convection in vertical channels. *J. Thermophys. Heat Transfer*, **3**, 375–383

Habchi, S. and Acharya, S. 1986. Laminar mixed convection in a symmetrically or asymmetrically, heated vertical channel. *Numer. Heat Transfer*, **9**, 605–618

Harlow, F. H. and Welch, J. E. 1965. Numerical calculation of time-dependent viscous incompressible flow of fluid with free surface. *Phys. Fluids*, **8**, 2182–2189

Heaton, H. S., Reynolds, W. C., and Kays, W. M. 1964. Heat transfer in annular passages. Simultaneous development of velocity and temperature fields in laminar flow. *Int. J. Heat Mass Transfer*, **7**, 763–781

Ingham, D. B., Keen, D. J., and Heggs, P. J. 1988. Flows in vertical channels with asymmetric wall temperatures and including situations where reversal flows occur. *ASME J. Heat Transfer*, **110**, 910–917

Jeng, Y. N. and Chen, J. L. 1992. Truncation error analysis of the finite-volume method for a model steady convective equation. *J. Comput. Phys.*, in press

Mahmood, T. and Merkin, J. H. 1989. Mixed convection flow in narrow vertical ducts. *Wärme- und Stoffübertragung*, **24**, 257–271

Morton, K. W. and Paisley, M. F. 1989. A finite volume scheme with shock fitting for the steady Euler equations. *J. Comput. Phys.*, **80**, 168–203

Nieckele, A. O. and Azevedo, F. A. 1987. Reverse flow in one-sided heated vertical channels in natural convection. *Convective Transport*, **82**, 71–77 (Annual Meeting of ASME, Dec 16-18, 1987, Boston, ASME Heat Transfer Division)

Özisik, M. N. 1985. *Heat Transfer, A Basic Approach.* McGraw-Hill, New York, 268–269

Patankar, S. V. 1980. *Numerical Heat Transfer and Fluid Flow.* Hemisphere, Washington, DC

Shyy, W. 1985a. A study of finite difference approximations to steady-state, convection-dominated flow problems. *J. Comput. Phys.*, **57**, 415–438

Shyy, W. 1985b. Numerical outflow boundary condition for Navier–Stokes flow calculations by a Line iterative method. *AIAA J.*, **23**, 1847–1848

Shyy, W. 1987. Effects of open boundary on incompressible Navier–Stokes flow computation: numerical experiments. *Numer. Heat Transfer*, **12**, 157–178

Sorenson, R. L. and Steger, J. L. 1977. Simplified clustering of nonorthogonal grids generated by elliptic partial differential equations. *NASA TM* 73252 National Tech. Inform. Service, Springer, VA

Sparrow, E. M., Chrysler, G. M., and Azevedo, L. F. 1984. Observed flow reversals and measured-predicted Nusselt numbers for natural convection in a one-sided heated vertical channel. *ASME J. Heat Transfer*, **106**, 325–332

Turkel, E. 1986. Accuracy of schemes with nonuniform meshes for compressible fluid flows. *Appl. Numer. Math.*, **2**, 529–550

Vanka, S. P. 1987. Second order upwind differencing in a recirculating flow. *AIAA J.*, **25**, 1435–1441

Vinokur, M. 1989. An analysis of finite-difference and finite-volume formulations of conservation laws. *J. Comput. Phys.*, **81**, 1–52

Williams, P. G. 1975. A reverse flow computation in the theory of self-induced separation. *Proc. 4th International Conf. Numer. Meth. Fluid Dynam.*, Richtmyer, R. D. (ed.). *Lecture Notes in Physics*, **35**, 445

Wirtz, R. A. and McKinley, P. 1985. Buoyancy effects on downward laminar convection between parallel plates. In *Fundamentals of Forced and Mixed Convection*, Kulacki, F. A. and Boyd, R. D. (eds.), New York, Vol. 42. ASME, 105–112

Yao, L. S. 1983. Free and forced convection in the entry region of a heated vertical channel. *Int. J. Numer. Meth. Eng.*, **26**, 65–72

Appendix 1

After rewriting Equations 1 to 4 into integral forms, the corresponding discretized equations can be obtained by the finite-volume approximation (Jeng and Chen 1992). For the sake of clarity, the following model convective–diffusive equation with a source term is considered in order to demonstrate the finite-volume method,

$$\oint_S \phi \vec{V} \cdot d\vec{S} = \oint_S \Gamma \nabla\phi \cdot d\vec{S} + \int_v S^\phi \, dv \tag{A1}$$

where the left-hand side is the convective term, while the right-hand side includes the diffusive term and source term.

For rectangular cells as shown in Figure 2, the corresponding surface integrals can be expressed as

$$\oint_S d\vec{S} = \int_{Se} d\vec{S} + \int_{Sn} d\vec{S} + \int_{Sw} d\vec{S} + \int_{Ss} d\vec{S}$$
$$= \int_1^2 d\vec{S} + \int_2^3 d\vec{S} + \int_3^4 d\vec{S} + \int_4^1 d\vec{S} \tag{A2}$$

By discretizing Equation A1 via Equation A2, we obtain the following numerical expression for the convective term (Jeng and Chen 1992):

$$\oint_S \phi \vec{V} \cdot d\vec{S} = (\phi u)_e \Delta y_{12} - (\phi u)_w \Delta y_{43} + (\phi v)_n \Delta x_{32} - (\phi v)_s \Delta x_{41} - \text{T.E.} \tag{A3}$$

For the diffusive term and source terms, we have, respectively,

$$\oint_S \nabla\phi \cdot d\vec{S} = \Gamma_e(\phi_E - \phi_P)[\Delta y_{21}/\Delta x_{EP}] - \Gamma_w(\phi_P - \phi_w)[\Delta y_{43}/\Delta x_{WP}] + \Gamma_n(\phi_N - \phi_P)[\Delta x_{32}/\Delta y_{PN}] - \Gamma_s(\phi_P - \phi_S)[\Delta y_{41}/\Delta y_{SP}] - \text{T.E.} \tag{A4}$$

$$\int_v S^\phi \, dv = S_P^\phi \Delta x_{41} \Delta y_{12} - \text{T.E.} \tag{A5}$$

where T.E. indicates the corresponding truncation error.

Because of the stability consideration and locations of dependent variables being defined on nodal points (cell center), the values on the cell surfaces should be properly approximated from nearby nodal points. In this study, for Equation A3, the conventional second-order upwind scheme is employed to model properties on cell surfaces, namely,

$$(\phi u)_e = u_e(\tfrac{3}{2}\phi_P - \tfrac{1}{2}\phi_W) \qquad \text{for} \quad u_e \geqslant 0 \tag{A6}$$

Similar expressions are written for other surfaces.

Finally, the governing equations of Equations 2 to 4 are summarized in the following form:

$$A_P^\phi \phi_P = A_E^\phi \phi_E + A_W^\phi \phi_W + A_N^\phi \phi_N + A_S^\phi \phi_S + S^\phi. \tag{A7}$$

where ϕ can be u, v, θ, p, or p'. Subsequently, the SIMPLER algorithm (Patankar 1980) is employed to solve this set of equations.

Appendix 2

Let the arc length $S(\eta)|_\xi$ along a ξ = constant line be approximated as in Sorenson and Steger (1977):

$$S_0 = 0; \; S_j = S_{j-1} + \sqrt{(x_j - x_{j-1})^2 + (y_j - y_{j-1})^2} \qquad 1 \leqslant j \leqslant j_{\max} \tag{A8}$$

Consequently, a unique relation between the grid coordinates (x, y) and the arc length S is constituted. Next, introduce a stretching transformation along each constant ξ such that

$$\tilde{S}_0 = S_0; \; \tilde{S}_j = \tilde{S}_{j-1} + \Delta\tilde{S}_{\min}(1 + \varepsilon)^{j-2} \quad 1 \leqslant j \leqslant j_{\max} \tag{A9}$$

where $\Delta\tilde{S}_{\min}$ is the desired grid spacing next to the boundary, and ε is evaluated by Newton's iterative scheme so that $\tilde{S}_{\max} = S_{\max}$. After identifying $S_{i-1} \leqslant \tilde{S}_j \leqslant S_i$ for some i, the resulting grid coordinates (x_j, y_j) is evaluated by the linear interpolation formula.

In fact, if ε is small enough, the resulting grid stretching is an algebraic stretching (quasi-uniform grid) defined by Turkel (1986). He classifies a grid stretching as algebraic (or quasi-uniform) if

$$l_j = \frac{\tilde{S}_j - \tilde{S}_{j-1}}{\tilde{S}_{\max}} \tag{A10}$$

$$R_j = l_{j+1}/l_j = 1 + O(l^m), \; m > 0 \quad \text{and} \quad l = \max_j l_j \tag{A11}$$

where a larger m corresponds to a smoother grid stretching. Using Equation 20 and the definition of l_j, it is easy to get

$$R_j = l_{j+1}/l_j = 1 + \varepsilon \qquad \text{(A12)}$$

One can easily construct the grid system with $\varepsilon \sim O(l_j)$ or $O(l_j^2)$ to meet the requirement of Equation A11. Hence, the second-order upwind scheme as well as the diffusion scheme of the present simulation can preserve their order of accuracy (Jeng and Chen 1992).

Appendix 3

Tables A1 to A16 contain information for various Re values using Re = 200 as the standard. These tables give the results for various values of Gr/Re and r_t. The cases shown do not all involve flow separation. If no flow separation is found within the computational domain, the column L_s is marked with a star. Table A1 exhibits the same case as indicated in Table 1. The data of Table A1 show that when Re $\geqslant$ 50, the values of MAE and MSE are relatively small. By the previous argument, it is found that the approximate lower limit for Reynolds number independence is once again about Re $\sim$ 50.

Table A1 Comparison of discrepancy for various Re numbers based on reference Re = 200 for Gr/Re = 300 and $r_t = 0.3$

Re	L_X	MAE	MSE	IAE	L_s
1	0.1	0.31876	0.08851	0.20413	0.43233
10	0.1	0.04054	0.00406	0.03462	0.10658
25	0.1	0.00729	0.00073	0.00630	0.09474
50	0.1	0.00201	0.00011	0.00076	0.09244
75	0.1	0.00217	0.00011	0.00048	0.09221
100	0.1	0.00176	0.00011	0.00053	0.09211
150	0.1	0.00080	0.00005	0.00038	0.09200
200	0.1				0.09213
300	0.067	0.00121	0.00008	0.00059	*
500	0.04	0.00256	0.00020	0.00150	*
1000	0.04	0.00401	0.00034	0.00221	*

Table A2 Comparison of discrepancy for various Re numbers based on reference Re = 200 for Gr/Re = 0 and $r_t = 0.3$

Re	L_X	MAE	MSE	IAE	L_s
1	0.1	0.23189	0.06550	0.15235	*
10	0.1	0.02066	0.00322	0.01348	*
50	0.1	0.00664	0.00054	0.00353	*
100	0.1	0.00365	0.00026	0.00196	*
150	0.1	0.00146	0.00009	0.00078	*
200	0.1				*

Table A3 Comparison of discrepancy for various Re numbers based on reference Re = 200 for Gr/Re = 100 and $r_t = 0.3$

Re	L_X	MAE	MSE	IAE	L_s
1	0.1	0.26991	0.07533	0.17438	*
10	0.1	0.03085	0.00377	0.02436	*
50	0.1	0.00450	0.00030	0.00147	*
100	0.1	0.00261	0.00017	0.00116	*
150	0.1	0.00107	0.00007	0.00050	*
200	0.1				*

Table A4 Comparison of discrepancy for various Re numbers based on reference Re = 200 for Gr/Re = 500 and $r_t = 0.3$

Re	L_X	MAE	MSE	IAE	L_s
1	0.1	0.35288	0.09820	0.22615	0.36043
10	0.1	0.04641	0.00643	0.04098	0.09400
50	0.1	0.00279	0.00023	0.00198	0.08026
100	0.1	0.00123	0.00007	0.00044	0.07961
150	0.1	0.00105	0.00005	0.00039	0.07954
200	0.1				0.07941

Table A5 Comparison of discrepancy for various Re numbers based on reference Re = 200 for Gr/Re = 0 and $r_t = 0.0$

Re	L_X	MAE	MSE	IAE	L_s
1	0.1	0.17828	0.05036	0.11713	*
10	0.1	0.01591	0.00248	0.01036	*
50	0.1	0.00511	0.00042	0.00273	*
100	0.1	0.00281	0.00020	0.00151	*
200	0.1				*

Table A6 Comparison of discrepancy for various Re numbers based on reference Re = 200 for Gr/Re = 100 and $r_t = 0.0$

Re	L_X	MAE	MSE	IAE	L_s
1	0.1	0.23742	0.06419	0.14746	0.61054
10	0.1	0.03418	0.00421	0.02711	0.13391
50	0.1	0.00298	0.00018	0.00106	0.11694
100	0.1	0.00187	0.00011	0.00072	0.11607
200	0.1				*

Table A7 Comparison of discrepancy for various Re numbers based on reference Re = 200 for Gr/Re = 300 and $r_t = 0.0$

Re	L_X	MAE	MSE	IAE	L_s
1	0.1	0.31846	0.08340	0.18909	0.31182
10	0.1	0.05896	0.00725	0.04657	0.06475
50	0.1	0.01348	0.00089	0.00763	0.04893
100	0.1	0.01132	0.00055	0.00577	0.04822
200	0.1				0.04692

Table A8 Comparison of discrepancy for various Re numbers based on reference Re = 200 for Gr/Re = 500 and $r_t = 0.0$

Re	L_X	MAE	MSE	IAE	L_s
1	0.075	0.27977	0.08817	0.16289	0.25812
10	0.075	0.05840	0.00841	0.04836	0.05529
50	0.075	0.00543	0.00058	0.00456	0.03983
100	0.075	0.00090	0.00007	0.00072	0.03880
200	0.075				0.03853

Table A9 Comparison of discrepancy for various Re numbers based on reference $\widetilde{Re} = 200$ for $Gr/Re = 0$ and $r_t = 0.5$

Re	L_X	MAE	MSE	IAE	L_s
1	0.1	0.26750	0.07556	0.17576	*
10	0.1	0.02385	0.00372	0.01556	*
50	0.1	0.00767	0.00063	0.00407	*
100	0.1	0.00421	0.00030	0.00226	*
200	0.1				*

Table A10 Comparison of discrepancy for various Re numbers based on reference $\widetilde{Re} = 200$ for $Gr/Re = 100$ and $r_t = 0.5$

Re	L_X	MAE	MSE	IAE	L_s
1	0.1	0.29910	0.08448	0.19603	*
10	0.1	0.03177	0.00383	0.02483	*
50	0.1	0.00535	0.00039	0.00211	*
100	0.1	0.00306	0.00021	0.00143	*
200	0.1				*

Table A11 Comparison of discrepancy for various Re numbers based on reference $\widetilde{Re} = 200$ for $Gr/Re = 300$ and $r_t = 0.5$

Re	L_X	MAE	MSE	IAE	L_s
1	0.1	0.34570	0.09827	0.22744	0.59673
10	0.1	0.04351	0.00564	0.03626	0.15415
50	0.1	0.00295	0.00021	0.00162	0.13550
100	0.1	0.00211	0.00015	0.00104	0.13475
200	0.1				*

Table A12 Comparison of discrepancy for various Re numbers based on reference $\widetilde{Re} = 200$ for $Gr/Re = 500$ and $r_t = 0.5$

Re	L_X	MAE	MSE	IAE	L_s
1	0.1	0.24531	0.10771	0.14448	0.48991
10	0.1	0.04912	0.00771	0.03752	0.12864
50	0.1	0.00261	0.00016	0.00097	0.11000
100	0.1	0.00111	0.00014	0.00024	0.10937
200	0.1				*

Table A13 Comparison of discrepancy for various Re numbers based on reference $\widetilde{Re} = 200$ for $Gr/Re = 0$ and $r_t = 1.0$

Re	L_X	MAE	MSE	IAE	L_s
1	0.1	0.35677	0.10077	0.23439	*
10	0.1	0.03181	0.00496	0.02074	*
50	0.1	0.01022	0.00083	0.00543	*
100	0.1	0.00561	0.00040	0.00301	*
200	0.1				*

Table A14 Comparison of discrepancy for various Re numbers based on reference $\widetilde{Re} = 200$ for $Gr/Re = 100$ and $r_t = 1.0$

Re	L_X	MAE	MSE	IAE	L_s
1	0.1	0.35405	0.10032	0.23347	*
10	0.1	0.02911	0.00453	0.01899	*
50	0.1	0.01027	0.00087	0.00580	*
100	0.1	0.00561	0.00041	0.00312	*
200	0.1				*

Table A15 Comparison of discrepancy for various Re numbers based on reference $\widetilde{Re} = 200$ for $Gr/Re = 300$ and $r_t = 1.0$

Re	L_X	MAE	MSE	IAE	L_s
1	0.1	0.34899	0.09950	0.23179	*
10	0.1	0.02362	0.00367	0.01544	*
50	0.1	0.01037	0.00095	0.00661	*
100	0.1	0.00561	0.00044	0.00340	*
200	0.1				*

Table A16 Comparison of discrepancy for various Re numbers based on reference $\widetilde{Re} = 200$ for $Gr/Re = 500$ and $r_t = 1.0$

Re	L_X	MAE	MSE	IAE	L_s
1	0.1	0.34402	0.09870	0.23014	*
10	0.1	0.01932	0.00284	0.01193	*
50	0.1	0.01047	0.00104	0.00742	*
100	0.1	0.00561	0.00046	0.00369	*
200	0.1				*